Available online at www.sciencedirect.com
ScienceDirect
Comput. Methods Appl. Mech. Engrg. 403 (2023) 115729
Computer methods in applied mechanics and engineering
www.elsevier.com/locate/cma

A new monolithic design approach for topology optimization for transient fluid–structure interaction system

Gil Ho Yoon

School of Mechanical Engineering, Hanyang University, Seoul, South Korea

Received 24 May 2022; received in revised form 27 September 2022; accepted 18 October 2022
Available online 10 November 2022

Abstract

This study presents a new topology optimization method for transient coupled fluid–structure interaction (FSI) problems. The transient FSI problem is formulated using the monolithic design approach combining the design variables and the governing equations. This new approach allows for the possibility of considering the effect of transient FSI on topologically optimized layouts. Throughout this work, the analysis domain for the fluid and structure is modeled using the unified monolithic approach, in which the structure equation and the Navier–Stokes equation are coupled. With a fixed mesh and design variables assigned to each finite element, the governing equations as well as the involved material properties are interpolated. This modeling and analysis approach provides accurate solutions to the strongly coupled FSI system. An adjoint approach for calculating the transient sensitivity information and a gradient-based optimizer are used. Several numerical examples are solved to reveal the importance of considering the transient FSI. In addition, these examples demonstrate that the present approach can control transient FSI phenomena.

Keywords: Topology optimization; Transient FSI; Monolithic design approach; Transient boundary condition; Transient sensitivity analysis

1. Introduction

A new topology optimization method for the transient coupled fluid–structure interaction (FSI) problem is developed in Fig. 1. Topolgoy optimization for transient FSI is a sophisticated and challenging subject as the interpolations of the governing equations and the material properties should be formulated with the spatially varying density variables. In the present study, transient FSI system is formulated and solved by the monolithic design approach combining the design variables and the governing equations with the deformation tensor. The governing equations and the material properties can be interpolated with a fixed mesh and the design variables assigned to each finite element. This modeling and analysis approach provides accurate solutions to the strongly coupled governing equations without an explicit boundary definition. A transient adjoint approach for evaluating the sensitivity information and a gradient-based optimizer are employed. Several optimization problems are considered to reveal the importance of considering the transient FSI.

Since the innovative development of the structural topology optimization scheme mainly minimizing structural compliance subject to a mass constraint, various optimization methods and schemes have been presented and applied

E-mail address: ghy@hanyang.ac.kr.

https://doi.org/10.1016/j.cma.2022.115729
0045-7825/

to challenging engineering applications (see [1–4] and references therein). In addition to structural optimization problems or related problems, several studies have been carried out for fluid-related problems. A comprehensive review of the topology optimization of fluid can be found [5–7]. In [8], the innovative topology optimization of unsteady incompressible Navier–Stokes flows was developed. The transient sensitivity of the fluid was rigorously presented and the calculus of variation is applied for the rigorous sensitivity analysis which is employed in the present study. In [9], a variational level-set method for steady-state Navier–Stokes flow was proposed. With an explicit expression of boundary, it is possible to carry out fluid optimization. For the sensitivity analysis, a variational form was formulated with Lagrangian multiplier technique. In [10], the lattice Boltzmann method in which a fluid density on a lattice is simulated was applied to the topology optimization for multicomponent flow. Compared with classical finite volume or finite element methods, the lattice Boltzmann method solves the fluid problem by calculating the distribution function. In [6], a density based topology optimization was developed using a open source code (OpenFOAM software). With this developed, a fluid topology optimization with a large scale domain can be solved efficiently. In [11,12], innovative fluid optimization frameworks with OpenFOAM and FENICS were presented. In [7], the TOBS (Topology optimization of binary structure) is presented for the optimization of high Reynolds fluid flow analysis. Through this research, the optimization problem with the discrete design variables is solved. It is expected that this approach can resolve the intermediate design variable issue in complex fluid topology optimization problem. In [13], the discrete adjoint approach was developed in combination with a finite differences scheme for the sensitivity analysis. It is expected that this research can disseminate the fluid optimization for various engineering fields. In [14], the topology optimization with two fluid heat exchange is carried out. In [15], topology optimization for the fluid domain using kinetic theory was investigated. In connection with the researches of laminar flow, turbulent flow has become an emerging topic too. The sensitivity of turbulent flow was investigated in [16]. In [17], topology optimization for a 3D rotor flow path design was developed. In [18,19], turbulent flow was considered in topology optimization using the RANS models. They revealed that the turbulent viscosity is modeled and added in the simulation and topology optimization. One of the difficulties is that the sensitivity analysis becomes complex. In addition, the conjugate heat transfer problem is also one of the important subjects related to the topology optimization for fluids. In [20–28], the topology optimization for conjugate heat transfer problem was considered. In [29], three-dimensional fluid topology optimization for heat transfer system was developed. Optimization scheme for electromechanical systems was presented in [30]. In [31], a level-set approach for the heat conduction problem was also developed. In [32], natural convection was considered in topology optimization. In [33], a graded porous structure was used as the heat-dissipation structure. Recently, optimization research on the motion of particles suspended in a fluid has gained importance. In [34], the trajectory of a particle suspended in a fluid was optimized using topology optimization. In [35], a framework for the topology optimization of a particle manipulator was presented. These researches can be extended to consider the particle motions in fluid and show the prominent results for the development of micro fluid devices.

Access to the well-developed finite element theory and optimized theory for multiphysics problems becomes important. Based on the developments in topology optimization for fluid, there are numerous works that discuss enhancements of FSI systems. The application of fluid–structure interaction can be found in many engineering applications such as aircraft, spacecraft, bioengineering and automobile. For examples, while designing aircraft wings or turbine blades, the failure due to FSI oscillation should be considered. For the container design, the fluid–structure interaction needs to be considered to prevent excessive liquid oscillation too. The lubrication between bearings and gears is also one of FSI examples. In bioengineering, the FSI is needed to model blood flow. In the framework of the density based topology optimization for FSI, the most difficult aspect is that the spatially varying design variables should interpolate the two governing equations in addition to the material properties. To cope with this difficulty, the monolithic design formulation was proposed for topology optimization for a steady-state and stationary FSI structure in [36]. In the approach, the continuity in force is imposed by applying the divergence theory. In other words, the surface force is transferred to the volume force in the monolithic design approach. While developing the theory, it is important to ensure the accuracy of the developing theory by comparing the solutions (displacement, stress, fluid velocity, and pressure). By considering the fluid work to structure, some modifications are made in the monolithic design formulation. Then, stress-based topology optimization for the FSI structure was developed in the framework of the monolithic design approach in [37]. With the existing procedures, the optimization for FSI is also possible. In [38], the fluid–thermal–structural interaction was researched. In [39,40], the levelset based topology optimization scheme with body-fitted mesh was developed. In [41], a level-set-based topology optimization

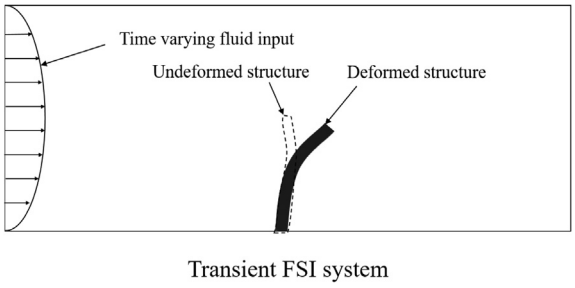

Fig. 1. Topology optimization of transient fluid–structure interaction.

scheme for stationary FSI problems was developed. The topology optimization of coupled multiphysics problems was presented in [42,43]. In [44,45], topology optimization with binary design variables was proposed for design-dependent FSI structures. In [46], a topology optimization scheme for a thermal FSI system was developed using a body-fitted mesh and parallel computing. In short, structural optimization of FSIs is a challenging and important subject in engineering. To our best knowledge, the monolithic design approach is extended for the transient FSI structure for the first time in the present study.

This study adopts and expands the monolithic design approach [36]. The monolithic design approach modifies the fluid and structural equations to allow topological alteration. In the linear elasticity equation, a weak Young's modulus is assigned to simulate fluid domain. In the Navier–Stokes equation, a large Darcy force is assigned to structural domain. With this assignment, the fluid velocities of the structural domain become very small and can be negligible from an engineering perspective. In this approach, the continuity conditions in traction and velocity are naturally imposed along the interface boundary between solid and fluid. Although it is difficult to interpret the physical states with the design variables, it is possible to represent the physical phenomena of FSI with converged design variables, that is, ones or zeros. To consider the transient effect, this study formulates transient monolithic equations by adding the inertia terms to the governing equations. The design variables are defined at each finite element, and the variational principle is used for the sensitivity analysis of the integration of the transient compliance considering the FSI. A gradient-based optimizer is used for the optimization. Several examples are considered to verify the developed approaches. To maximize the effect of the transient FSI phenomenon on optimized layout, time-varying fluid inputs are considered.

The remainder of this paper is organized as follows. Section 2 provides the mathematical formula pertaining to the coupled analysis of the transient structure and transient fluid motions and the development of the sensitivity analysis of the integration of the transient compliance. Section 3 describes several topology optimization examples that test the effect of a transient fluid and demonstrate its importance. Section 4 presents the conclusions of the study and provides suggestions for future research.

2. Transient fluid–structure interaction with the monolithic design approach

In this section, the development of the transient topology optimization scheme and the multiphysics and monolithic analysis coupling between the transient Navier–Stokes equation and the transient elastodynamics are presented. For the optimization formulation, the dynamic compliance was set as the objective, and the volume was constrained. Transient sensitivity analysis based on the calculus of variation was employed (see Fig. 2).

The FSI system is interesting and challenging from a mathematical perspective. Although advanced computational optimization approaches may achieve better performance than human performance for the optimization of multiphysics systems, several high-performing finite element analysis theories are difficult to apply in topology optimization. Depending on the coupling approach, monolithic and staggered analysis procedures have been proposed. In the framework of density-based topology optimization, the existing analysis procedures, either monolithic or staggered, are difficult to apply. To cope with this difficulty for the topology optimization, one approach may be the application of a topology optimization scheme with an explicit boundary [41–43]. In this study, the topology optimization method with spatially varying design variables was applied in cooperation with the monolithic analysis procedure.

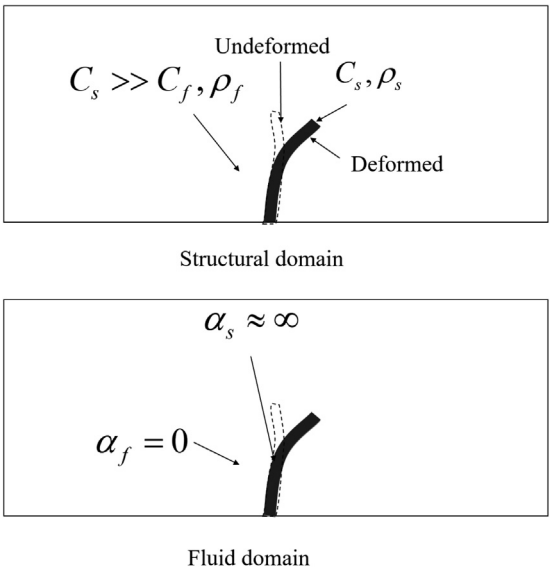

Fig. 2. Material interpolation scheme in the monolithic design approach.

The *monolithic design procedure* for FSI was proposed in [36] to consider the spatially varying or interpolated governing equations with respect to the change in the design variables as shown in Fig. 2. In other words, by changing the design variables, not only the material properties involving the governing equations but also the governing equations should be interpolated. Appropriate boundary conditions (continuity conditions of traction and displacement) should be applied along the coupling boundary of the fluid-interaction system. Because this procedure is intricate for the conventional analysis procedure, the *monolithic design approach* incorporating the design variables with the governing equations to interpolate the governing equations, that is, solid and fluid, was proposed using the deformation tensor and divergence theory [36]. The undeformed state, ${}^0\Omega$, and deformed state, ${}^t\Omega$, are recognized by the deformation tensor, $\mathbf{F}$.

$$\mathbf{F} = \frac{\partial \mathbf{x}}{\partial \mathbf{X}} \tag{1}$$

where the positions of the undeformed and the deformed domains are denoted as $\mathbf{X}$ and $\mathbf{x}$, respectively. Using the deformation tensor, the differential and integral operators can be transferred as follows:

$$\nabla_{\mathbf{X}} = \mathbf{F}^{\mathrm{T}} \nabla_{\mathbf{x}}, \ \ \nabla_{\mathbf{x}} = \mathbf{F}^{-\mathrm{T}} \nabla_{\mathbf{X}} \tag{2}$$

The governing equation of linear dynamic structure is defined as follows:

$$\nabla_{\mathbf{x}} \cdot \mathbf{T}_s + \mathbf{F} = \rho_s \ddot{\mathbf{u}} \text{ in } {}^t\Omega \tag{3}$$

where the structural tensor and structural displacements are denoted as $\mathbf{T}_s$ and $\mathbf{u}$, respectively. The force and inertial forces are denoted by $\mathbf{F}$ and $\rho_s \ddot{\mathbf{u}}$, respectively. The structural density is denoted by ρ_s.

One of the main differences in the monolithic design approach for FSI lies in the fact that the fluid equation and structural equation exist for an entire analysis domain (${}^0\Omega$ or ${}^t\Omega$). The classical monolithic and staggered analysis procedures distinguish the fluid and structural domains. Considering the virtual work principle, the weak form of the structural equation can be expressed as follows:

$$-\int_{{}^0\Omega} \rho_s \delta \mathbf{u}^{\mathrm{T}} \ddot{\mathbf{u}} - \int_{{}^0\Omega} \delta \mathbf{S}^{\mathrm{T}} \cdot \mathbf{T}_s d\Omega + \int_{{}^0\Omega} \Psi \cdot \mathbf{F}^{-\mathrm{T}} \delta \mathbf{S}(\mathbf{u}, \delta \mathbf{u})^{\mathrm{T}} \cdot p \, \|\mathbf{F}\| \, d\Omega + \int_{{}^0\Omega} \Psi \cdot \mathbf{F}^{-\mathrm{T}} \delta \mathbf{u} \cdot \nabla_{\mathbf{X}} p \, \|\mathbf{F}\| \, d\Omega = \mathbf{0} \tag{4}$$

$$\delta \mathbf{S} = \frac{1}{2}(\nabla_{\mathbf{X}} \delta \mathbf{u} + \nabla_{\mathbf{X}} \delta \mathbf{u}^{\mathrm{T}}), \tilde{\mathbf{S}}(\mathbf{u}, \delta \mathbf{u}) = \frac{1}{2}(\nabla_{\mathbf{x}} \delta \mathbf{u} + \nabla_{\mathbf{x}} \delta \mathbf{u}^{\mathrm{T}}) \tag{5}$$

The virtual displacements are denoted by $\delta\mathbf{u}$, and the virtual and auxiliary virtual strains are denoted by $\tilde{\mathbf{S}}$ and $\tilde{\mathbf{S}}(\mathbf{u}, \delta\mathbf{u})$, respectively. The mutual coupling condition from the point of view of the linear elastodynamic equation is imposed by divergence theory. The Young's modulus and density of the structure are interpolated with respect to the design variables γ_e as follows:

$$\begin{aligned} C(\gamma_e) &= C_S\gamma_e^n + C_f(1-\gamma_e^n) \\ \rho(\gamma_e) &= \rho_S\gamma_e^{n_s} + \rho_{void}(1-\gamma_e^{n_s}),\ \rho_{void} \ll \rho_S \end{aligned} \tag{6}$$

where the Young's moduli of the structure and fluid are denoted as C_S and C_f, respectively. The density values of the structure and void are denoted as ρ_s and ρ_{void}, respectively. Penalization factors are denoted by n and n_s. To remove local oscillations, the value of n_s is set to be higher than that of n. Depending on the penalization factor, various local optima can be obtained. The window function Ψ is defined to convert the boundary integration (fluid force exerted on the structure) to domain integration.

$$\Psi = \gamma_e^{n_{filter}} \tag{7}$$

The penalization factor for the window is n_{filter}. For the monolithic equation, the pseudo-rigid domain is commonly defined using the Darcy force. To simulate the transient motions of the fluid, the following transient incompressible fluid equations defined in the deformed domain, ${}^t\Omega$, are formulated:

$$\rho_f\frac{\partial\mathbf{v}}{\partial t} + \rho_f(\mathbf{v}\cdot\nabla_{\mathbf{x}})\mathbf{v} = \nabla_{\mathbf{x}}\cdot\left[-p\mathbf{I} + \mu(\nabla_{\mathbf{x}}\mathbf{v} + \nabla_{\mathbf{x}}\mathbf{v}^{\mathrm{T}})\right] - \alpha\mathbf{v} \quad \text{on} \quad {}^t\Omega \tag{8}$$

$$\nabla_{\mathbf{x}}\cdot(\rho_f\mathbf{v}) = 0 \tag{9}$$

The analysis domain is denoted as Ω_t, which simultaneously contains the fluid equations and the elastodynamic equation. The fluid inertia term is added at the beginning of the governing equation, and at the end of the transient Navier–Stokes equation (8), the Darcy force formulated with the design variables of the topology optimization is included. For finite element analysis, it is necessary to derive the weak forms of the governing equations in the undeformed domain using structural displacements $\mathbf{u}$. To numerically simulate the pseudo-rigid domain (the non-permissible domain) with respect to the spatially varying design variables, the Darcy force simulated with the SIMP method is formulated [8,34,35].

$$\alpha(\gamma_e) = \alpha_{\max}\gamma_e^{n_{per}} \tag{10}$$

The maximum value of permeability is $\alpha_{\max}$, and the penalization factor is n_{per}. Another interpolation can be employed for the interpolation of the Darcy force with respect to the design variables. In the present study, the SIMP interpolation function is employed without the loss of generality. In the Navier–Stokes equation, the necessity of the interpolation of the fluid density should be mentioned. In fluid simulation, with the sufficient large Darcy's force, the interpolation of the fluid density is not definitely necessary. However, the interpolation of the fluid density does improve the convergence of the simulation as the fluid inertia force becomes small in solid domain. Although not presented, the interpolation of fluid density was tested and we could get similar results. In connection to this, it is also interesting to consider the necessity of the interpolation of the fluid viscosity which corresponds to the Young's modulus in the elasticity equation. Using the above function, the weak forms of the transient fluid equation can be expressed as follows:

$$\begin{aligned} &\int_{0\Omega}\delta\mathbf{v}^{\mathrm{T}}\rho_f\frac{\partial\mathbf{v}}{\partial t}d\Omega + \int_{0\Omega}\delta\mathbf{v}^{\mathrm{T}}\left\{\rho(\mathbf{v}\cdot\mathbf{F}^{-\mathrm{T}}\nabla_{\mathbf{X}}\mathbf{v})\right\}\|\mathbf{F}\|\,d\Omega = \\ &-\int_{0\Omega}\mathbf{F}^{-\mathrm{T}}\nabla_{\mathbf{X}}\delta\mathbf{v}^{\mathrm{T}}\mathbf{T}_f\,\|\mathbf{F}\|\,d\Omega - \int_{0\Omega}\alpha\delta\mathbf{v}^{\mathrm{T}}\mathbf{v}\,\|\mathbf{F}\|\,d\Omega + \int_{0\Gamma_{p^*}}\delta\mathbf{v}^{\mathrm{T}}p_{p^*}\mathbf{n}d\Gamma \end{aligned} \tag{11}$$

$$-\int_{0\Omega}\delta p^{\mathrm{T}}\{\nabla_{\mathbf{x}}\cdot\mathbf{v}\}\,\|\mathbf{F}\|\,d\Omega = 0 \tag{12}$$

The virtual velocities and pressure are denoted as $\delta\mathbf{v}$ and $\delta\mathbf{p}$, respectively. The pressure input condition, $p = p^*$, is defined at ${}^0\Gamma_{p^*}$. The above equations are solved using the second-order element for $\mathbf{u}$ and $\mathbf{v}$ and the first-order element for p.

For the gradient-based optimizer, it is necessary to derive a sensitivity analysis. The adjoint sensitivity analysis procedure is then derived.

$$\begin{aligned}\mathcal{L}(\mathbf{u}, \mathbf{v}, p, \gamma) &= J(\mathbf{u}, \nabla\mathbf{u}; \gamma) \\ &+ \int_0^{t_f} \int_{0_\Omega} \left(\mathbf{u}^a, \mathbf{v}^a, p^a\right)\mathbf{FS}(\mathbf{u}, \nabla\mathbf{u}, \mathbf{v}, \nabla\mathbf{v}, p, \nabla p, \gamma) d\Omega dt\end{aligned} \tag{13}$$

where the column set of monolithic equations for the fluid and solid is denoted by **FS**. The objective function is denoted as $J(\mathbf{u}, \nabla\mathbf{u}; \gamma)$. For example, the domain integration of the time-varying compliance can be defined as follows:

$$J(\mathbf{u}, \nabla\mathbf{u}; \gamma) = \int_0^{t_f} \int_{0_\Omega} \mathbf{S}^{\mathrm{T}} \cdot \mathbf{T}_s d\Omega dt \tag{14}$$

The adjoint structural displacements and adjoint fluid velocities and pressures are denoted as $\mathbf{u}^a$, $\mathbf{v}^a$, and $\mathbf{p}^a$, respectively. The adjoint sensitivity analysis is performed using the calculus of variation.

$$\delta\mathcal{L} = \mathbf{0} \tag{15}$$

$$\begin{aligned}\delta\mathcal{L} = &\frac{\partial\mathcal{L}}{\partial\mathbf{u}} \cdot \delta\mathbf{u} + \frac{\partial\mathcal{L}}{\partial\nabla\mathbf{u}} : \nabla\delta\mathbf{u} + \frac{\partial\mathcal{L}}{\partial\mathbf{v}} \cdot \delta\mathbf{v} + \frac{\partial\mathcal{L}}{\partial\nabla\mathbf{v}} : \nabla\delta\mathbf{v} \\ &+ \frac{\partial\mathcal{L}}{\partial p} \cdot \delta p + \frac{\partial\mathcal{L}}{\partial\nabla p} : \nabla\delta p + \frac{\partial\mathcal{L}}{\partial\gamma} \cdot \delta\gamma = \mathbf{0}\end{aligned} \tag{16}$$

The adjoint equations can be derived by setting the terms associated with the primal variables to zeros and with proper boundary conditions (see [8] and references therein) as follows:

$$\frac{\partial\mathcal{L}}{\partial\mathbf{u}} \cdot \delta\mathbf{u} + \frac{\partial\mathcal{L}}{\partial\nabla\mathbf{u}} : \nabla\delta\mathbf{u} = \mathbf{0} \tag{17}$$

$$\frac{\partial\mathcal{L}}{\partial\mathbf{v}} \cdot \delta\mathbf{v} + \frac{\partial\mathcal{L}}{\partial\nabla\mathbf{v}} : \nabla\delta\mathbf{v} = \mathbf{0} \tag{18}$$

$$\frac{\partial\mathcal{L}}{\partial p} \cdot \delta p + \frac{\partial\mathcal{L}}{\partial\nabla p} : \nabla\delta p = \mathbf{0} \tag{19}$$

Note that the objective function is dependent only on the structural displacements, structural strains, and design variables, explicitly and implicitly. See [8] and references therein for the variational approach for sensitivity analysis of transient fluid problems. Indeed, the following sensitivity can be obtained by solving the above equations for the adjoint variables:

$$\frac{dJ}{d\gamma} = \frac{\partial J}{\partial\gamma} + \int_0^{t_f} \int_{0_\Omega} \left(\mathbf{u}^a, \mathbf{v}^a, p^a\right) \frac{\partial\mathbf{FS}}{\partial\gamma} d\Omega dt \tag{20}$$

To demonstrate the accuracy of the sensitivity analysis, the example in Fig. 3 shows a comparison of the sensitivity analysis values with the finite difference values for the ten points. The objective function is the integration of the time-varying compliance due to the time-varying fluid input on the left side. Owing to the fluid inlet, the internal solid structure deflects transiently. As illustrated, an accurate sensitivity analysis was obtained.

3. Optimization examples

To demonstrate the validity and importance of the present topology optimization considering transient FSI, this section presents several examples solved using the above monolithic approach. A sensitivity filter is applied to remove the checkerboard pattern. The method of moving asymptotes (MMA) algorithm is employed as an

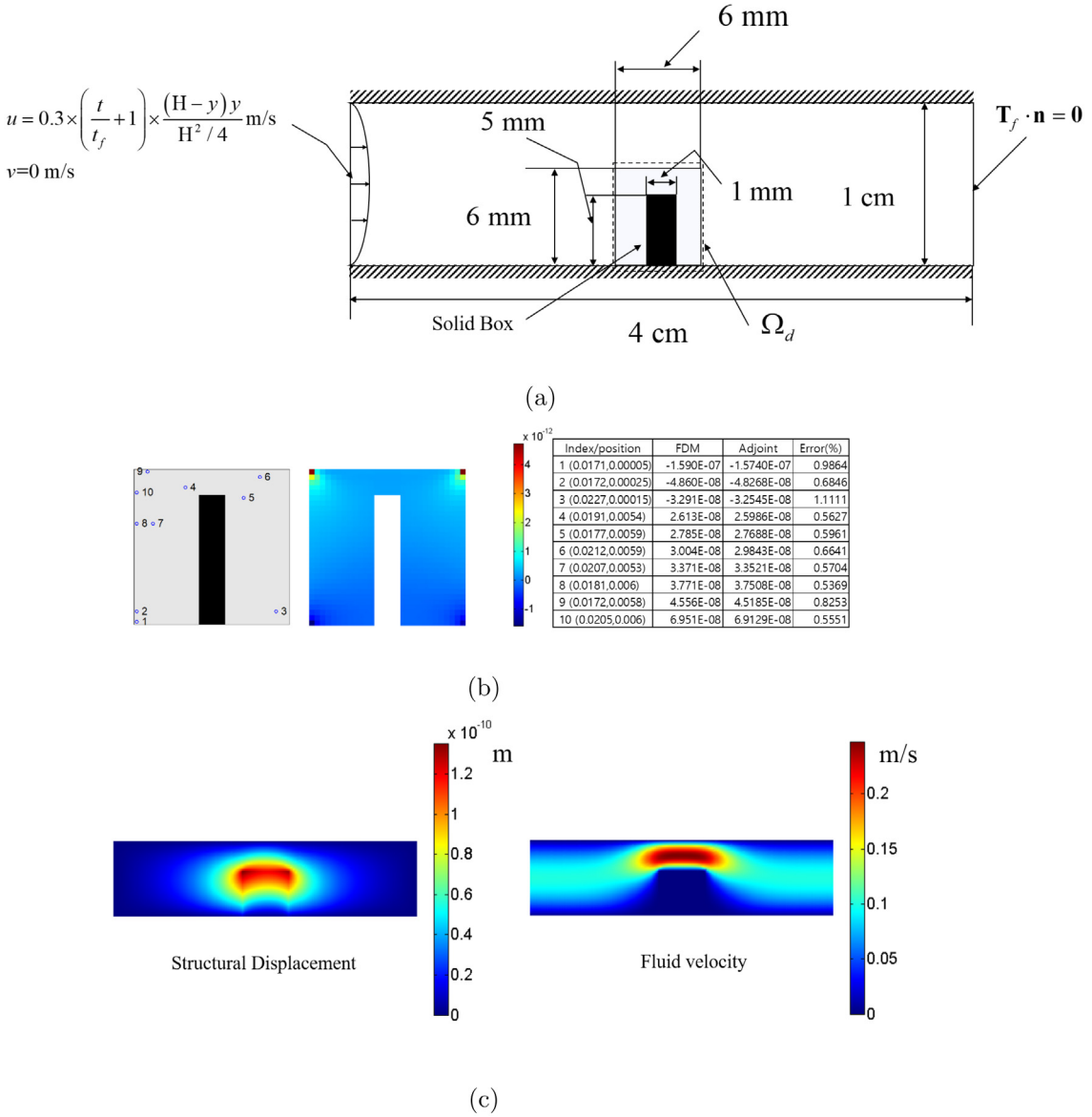

Fig. 3. Sensitivity analysis example ($\rho_s = 7800$ kg/m^3, Young's modulus: 200×10^9 Pa, $\rho_f = 1000$ kg/m^3, $\mu = 1$ Pa s, $\alpha_{\max} = 10^9$ Pa $\frac{s}{m^2}$, 60 by 60 mesh in the design domain, simulation time [0:0.0004:0.1] s, H = 1 cm, initial density distribution = 1, perturbation for finite difference method = 0.001).

optimization algorithm [47]. The optimization algorithm terminates when the convergence of the objective function falls below a specified threshold within one or two hundred iterations.

3.1. Example 1: Narrow channel problem

For the first example, the analysis and design domain shown in Fig. 3 is considered. Note that this problem was already considered in the previous work [36] and this research reconsiders this to verify the effect of the transient FSI structure. The inlet fluid flows from the left side toward the right side, and the magnitude of the parabolic fluid velocity along the input boundary condition is varied with respect to time. The optimization problem for FSI is

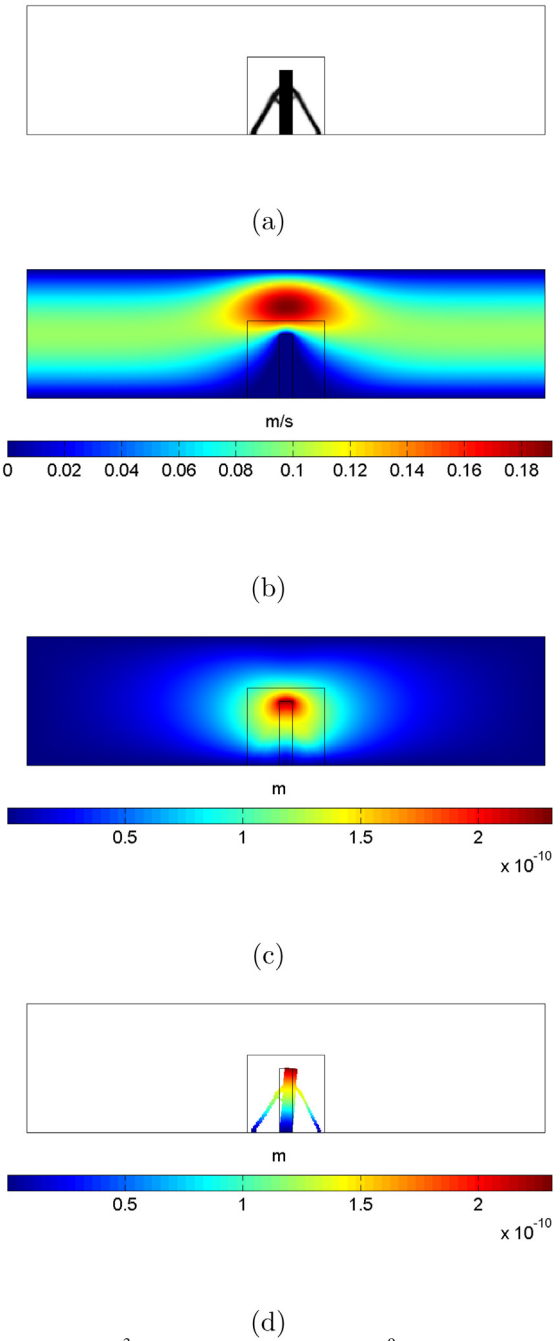

Fig. 4. Optimization result for 1 s ($\rho_s = 7800$ kg/m^3, Young's modulus: 200×10^9 Pa, $\rho_f = 1000$ kg/m^3, $\mu = 1$ Pa s, $\alpha_{\max} = 10^9$ Pa $\frac{s}{m^2}$, 60 by 60 mesh in the design domain, $u_{input} = u_0 \times t \times y \times (\mathrm{H} - y)/(\mathrm{H}/2)^2$, $u_0 = 0.1$ m/s, simulation time [0:0.1:1] s, $n = 3$, $n_s = 8$, $n_{filter} = 8$, $n_{per} = 8$). (a) Optimized layout with 10 percent mass usage with 0.01 for the initial value, (b) fluid velocity at 1 s, (c) structural deformation and (d) the scaled structural deformation only for structure (threshold value : 0.5).

formulated as follows:

$$\begin{aligned} &\min_{\gamma} \quad J = \int_0^{tf} \int_{0\Omega} \mathbf{S}^{\mathrm{T}} \cdot \mathbf{T}_{\mathrm{s}} \mathrm{d}\Omega \mathrm{d}t \\ &\text{Subject to} \sum_{e=1}^{N_e} \gamma_e \mathrm{v}_e \leq \mathrm{mass}_0 \\ &\gamma = [\gamma_1, \gamma_2, \ldots, \gamma_{N_e}], \quad \gamma_{\min} \leqslant \gamma \leqslant 1, \quad \gamma_{\min} = 0.001 \end{aligned} \tag{21}$$

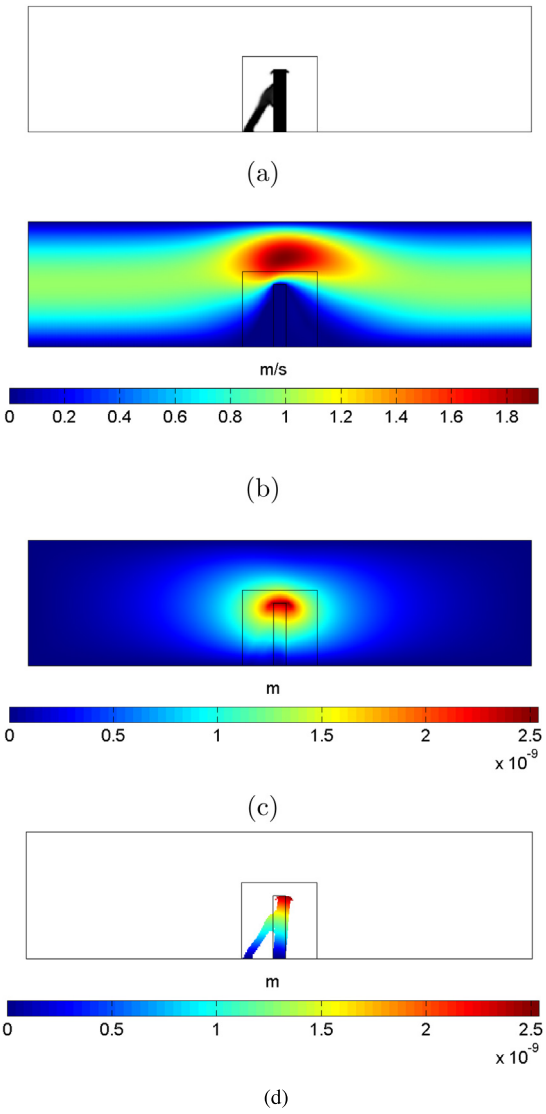

Fig. 5. Optimization result for 1 s with $u_{input} = u_0 \times t \times y \times (\mathrm{H} - y)/(\mathrm{H}/2)^2, u_0 = 1$ m/s. (a) Optimized layout with 10 percent mass usage, (b) fluid velocity at 1 s, (c) structural deformation and (d) the scaled structural deformation only for structure (threshold value : 0.5).

where N_e design variables are denoted by γ. The dependencies of the structural displacements, fluid velocities, and pressure in the objective function are considered explicitly and implicitly. A mass constraint is imposed with mass_0) for the upper bound of the structural mass. The volume of the eth element is v_e. The design variables are varied from the lower bound $\gamma_{\min}$ to the upper bound 1. As mentioned, the parabolic fluid input defined along the left side is assumed to have maximum velocity u_0. The effect of the maximum velocity of the fluid inlet on the optimal design is investigated. First, by setting 0.1 m/s (relatively slower flow) for u_0, it is assumed that the magnitude of the fluid inlet increases linearly with respect to time. With the present optimization framework and boundary conditions, the layout in Fig. 4(a) supporting the center structure can be obtained. An almost symmetrical design is obtained. The geometric properties of the optimized design are affected by many aspects. The envelop of the design is almost symmetric but the internal structure is unsymmetric. The fluid velocity and structural displacement are plotted in Fig. 4(b) and (c), respectively. To investigate the effect of the magnitude of the fluid velocity, it is increased to 1 m/s, as shown in Fig. 5. As the magnitude of the fluid velocity is increased by a factor of 10, the optimized layout in Fig. 5(a) supporting the front of the vertical solid bar is obtained. This optimized structure allows

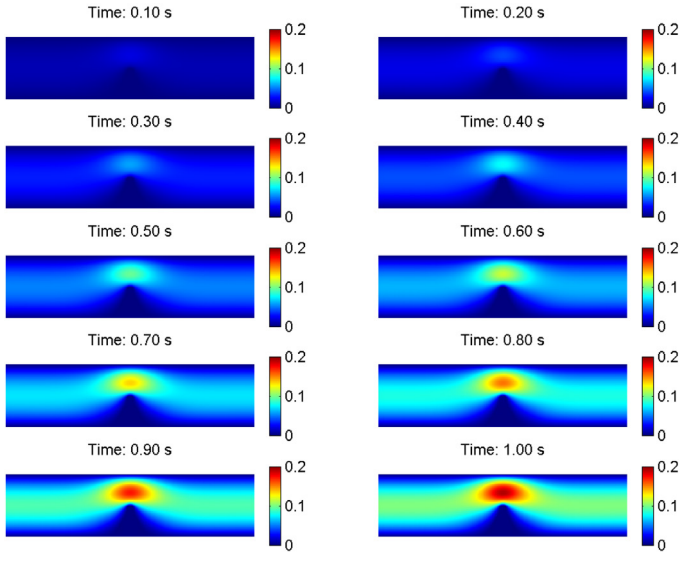

(a)

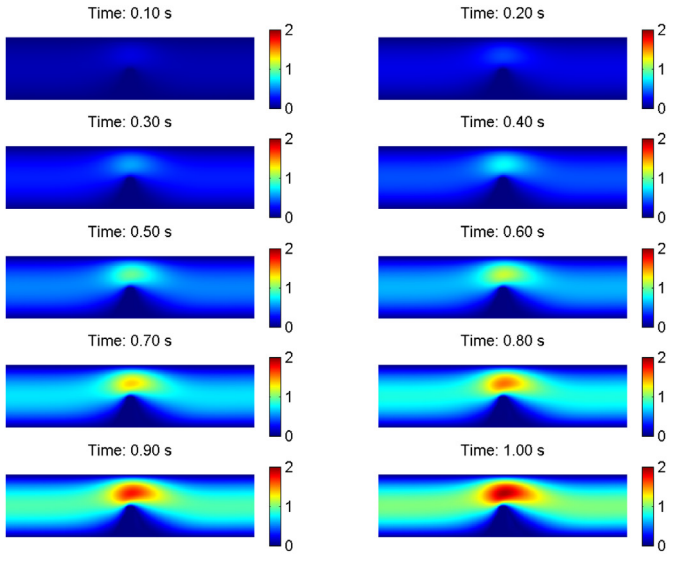

(b)

Fig. 6. Velocity comparison of the designs in Figs. 4 and 5.

smooth fluid flow over the vertical bar to minimize time-varying compliance. Note that with different penalization factors and boundary conditions, several different layouts can exist. Fig. 7 shows the convergence histories of the two designs. Fig. 6 compares the time-varying fluid velocities of the optimized layouts and Fig. 8 compares the compliance values of the two designs under each boundary condition. As illustrated, each design is optimized for each boundary condition.

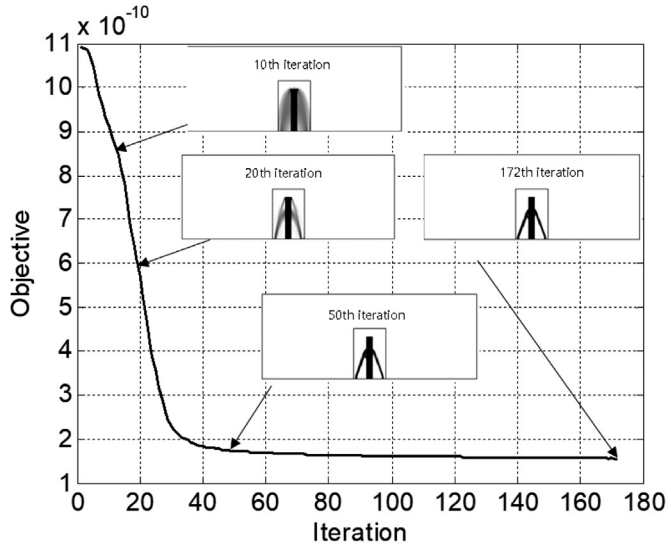

(a)

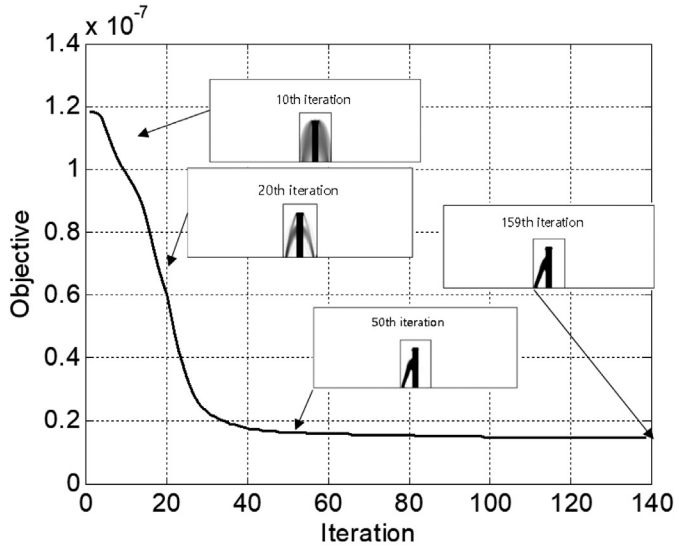

(b)

Fig. 7. Optimization histories.

3.2. Example 2: Optimization with two input inlets

For the second example, a rectangular design domain with a rectangular solid box at the center with time-varying fluid inputs along the left side is considered, as shown in Fig. 9. To further investigate the effect of the time-varying boundary condition on topology optimization, we consider two different fluid input conditions, that is, u_{in}^1 and u_{in}^2, at the upper and lower inlets along the left side. It is observed that the transient FSI effect may be magnified by different time-varying fluid inputs. The two fluid inputs are set as time-varying conditions in turn. For the first boundary condition, the fluid inputs (u_{in}^1 and u_{in}^2) increase linearly, whereas for the second optimization condition, one of

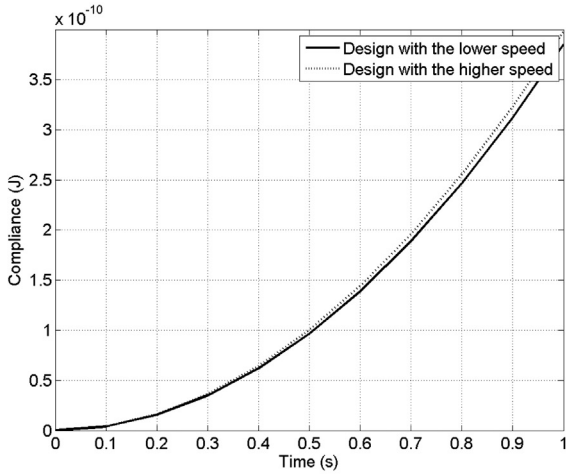

(a)

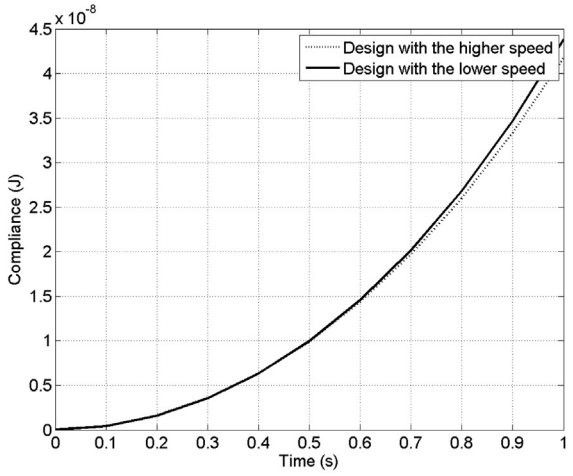

(b)

Fig. 8. Comparison of the responses of the two designs in Figs. 4 and 5. (a) Reanalysis of the two designs for the slower fluid inlet boundary condition and (b) reanalysis for the higher fluid inlet boundary condition.

the fluid inputs decreases linearly. The objective function is set to the integration of the time-varying compliance, as in (21), and a 10 percent mass constraint is considered. With the first linearly increasing fluid input over the time domain ([0:0.1:1] s), the straight design with the supporting structure in Fig. 10(a) can be obtained. As the time-varying fluid inputs simultaneously drag the center solid box toward the right side, as shown in Fig. 10(b) and (c), any object underneath or over the solid box increases the drag force, increasing the time-varying compliance. The channel design allowing the fluid input flow toward the right output boundaries is obtained; see the nozzle shape design in front of the rectangular box. To minimize the time-varying compliance without any disturbance of the fluid inputs, a supporting structure connecting the fixed boundary condition and solid box is obtained. Partially owing to the filtering scheme, some gray elements are observed. The fluid velocities and structural deformations are shown in Fig. 10(b) and (c), respectively. In contrast, a different boundary condition, that is, the linearly decreasing velocity input at the upper fluid input boundary, is imposed as shown in Fig. 11(a) and compared with the first fluid

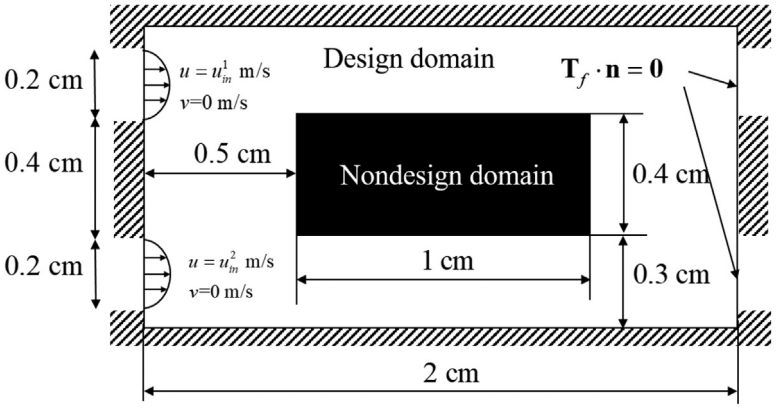

Fig. 9. Example 2: Problem definition with the two time-varying fluid inputs with a rectangular solid box (104 by 50 discretization, $\rho_s = 7800$ kg/m^3, Young's modulus: 200×10^9 Pa, $\rho_f = 1000$ kg/m^3, $\mu = 1$ Pa s, $\alpha_{\max} = 10^9$ Pa $\frac{\text{s}}{\text{m}^2}$, mass ratio: 10%, $n = 5$, $n_s = 5$, $n_{filter} = 8$, $n_{per} = 8$, Initial value $= 0.2$, 10% mass constraint).

boundary condition. The compliance values are monotonically increased due to the fluid velocities of the two inlets and their associated fluid forces are also increased in Fig. 11(a). On the other hand, the compliance curves become complex in Fig. 11(b) due to the decrease of the fluid velocity of the upper inlet. Compared with the fluid behavior and structural deformation in the first example, complex fluid motions in front of the solid box are observed, which cause bending deformation of the center solid structure. As the fluid inputs can now be mixed in front of the solid box, and the fluid input of one of the fluid input boundary conditions can flow to both fluid output conditions, the supporting structure appears at the rear of the solid box to prevent bending deformation. In addition, auxiliary ball-shaped structures are obtained at the left corners of the solid box.

Fig. 12 compares the time-varying compliance values of the two designs. In the optimization, the simulation time is set to 0–1 s with 0.1 s time interval, and the responses calculated with 0.01 s time interval are plotted in the figure. The compliance values of the two designs are monotonically increased in Fig. 12(a) for the boundary condition in Fig. 10. It is worth noting that the compliance response of the design in Fig. 12(b) is decreased until 0.5 s and then increased. The compliance is increased due to the fluid velocities of the two inlets and its associated fluid force are also increased in Fig. 12(a). On the other hand, the compliance curves become complex in Fig. 12(b) due to the decrease of the fluid velocity of the upper inlet.

This example shows that it is necessary to investigate the effect of the time-varying boundary condition and the local optima issue of the transient FSI system. The sharp decrease in Fig. 12(b) at the beginning of the simulation time is due to the pressure propagation speed. In Fig. 13, a refined mesh is adopted for the same problem. In case of the uniformly increased fluid inlets, the symmetric design in Fig. 13(a) is obtained. Owing to the mesh refinement, the symmetric supporting structures appear in front and at the rear of the rectangular solid box. For the asymmetrical fluid inlet condition, a similar structure is obtained and a dimple-shaped structure between the fluid inlets appears.

3.3. Example 3: Bend structure with two fluid inlets

For the next example of topology optimization for transient FSI, the design definition in Fig. 14 is considered. The optimization formulation minimizes the integration of the transient compliance subject to the mass constraint. Similar to the boundary conditions of the previous example, two fluid inlets are set and varied with respect to time. The fluids increase together smoothly, and the supporting structure appears in front of the internal solid box, as shown in Fig. 15. For the second boundary condition, the magnitude of the lower fluid inlet is decreased linearly, whereas that of the upper fluid inlet is increased linearly with respect to time. The supporting structure appears at the rear of the internal solid box, as shown in Fig. 16, unlike the first boundary condition. Fig. 17 shows the responses of the two designs for each boundary condition. As illustrated, each design is optimized for the given

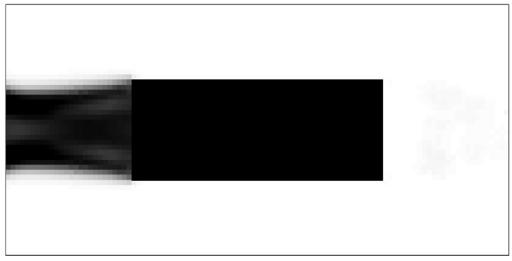

(a)

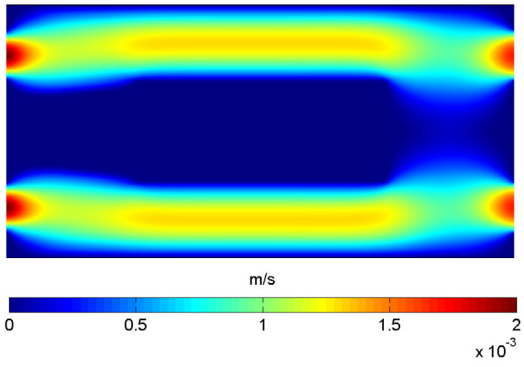

(b)

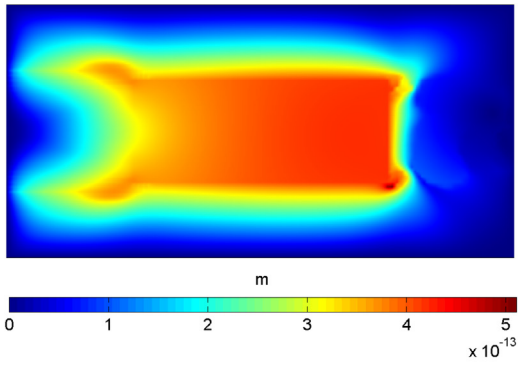

(c)

Fig. 10. Optimized layout with the boundary condition. (a) The optimized layout ($u_{in}^1 = u_0 \times t \times \frac{\left(3\times10^{-3}-y\right)\left(y-10^{-3}\right)}{\left(2\times10^{-3}\right)^2/4}$m/s, $u_{in}^2 = u_0 \times t \times \frac{\left(9\times10^{-3}-y\right)\left(y-7\times10^{-3}\right)}{\left(2\times10^{-3}\right)^2/4}$m/s, $u_0 = 2 \times 10^{-3}$ m/s, $n = 5$, $n_s = 8$, $n_{filter} = 5$, $n_{per} = 7$), (b) the fluid velocity and (c) the structural displacements.

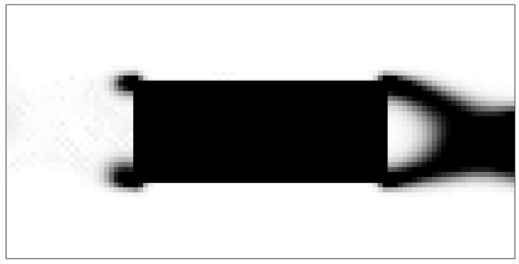

(a)

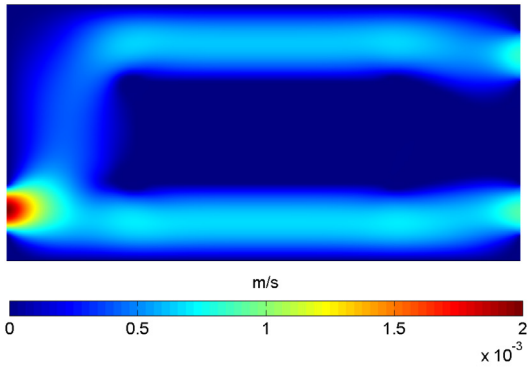

(b)

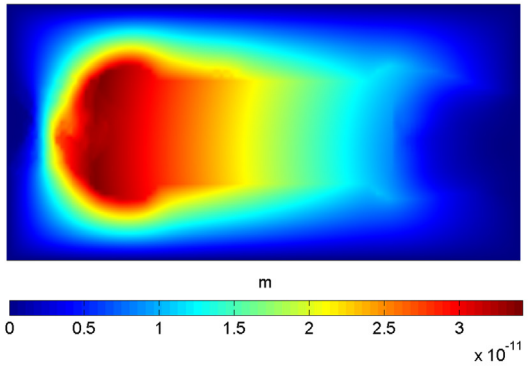

(c)

Fig. 11. Optimized layout with the boundary condition. (a) The optimized layout ($u_{in}^1 = u_0 \times t \times \frac{\left(3\times10^{-3}-y\right)\left(y-10^{-3}\right)}{\left(2\times10^{-3}\right)^2/4}$ m/s, $u_{in}^2 = u_0 \times (1-t) \times \frac{\left(9\times10^{-3}-y\right)\left(y-7\times10^{-3}\right)}{\left(2\times10^{-3}\right)^2/4}$ m/s, $u_0 = 2 \times 10^{-3}$ m/s), (b) the fluid velocity and (c) the structural displacements.

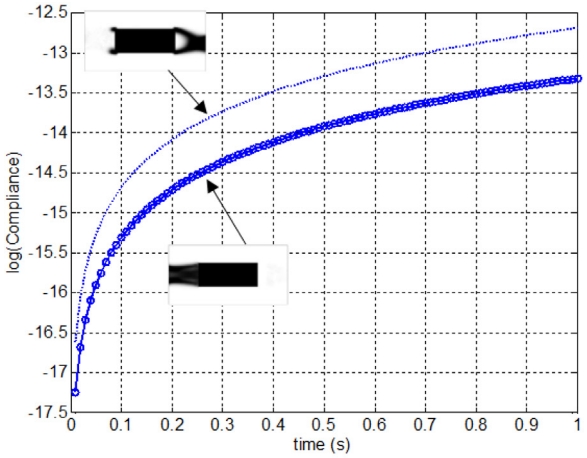

(a)

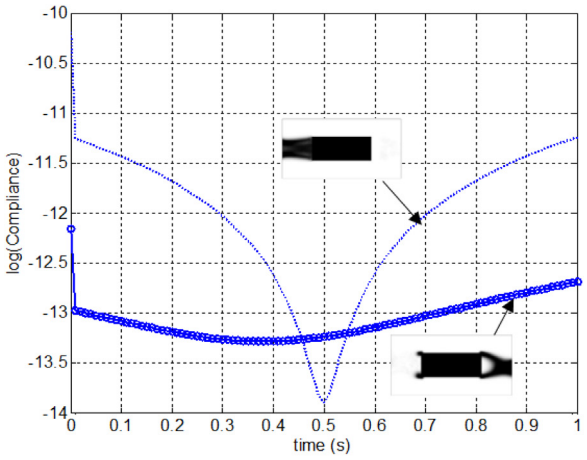

(b)

Fig. 12. Compliance comparison for each boundary condition. (a) Compliance values of the two designs with the boundary conditions shown in Fig. 10, and (b) compliance values of the two designs with the boundary conditions shown in Fig. 11.

boundary condition. In the designs, the gray elements are observed. It can be regarded as the side effect of the local optima in topology optimization. By investigating the distributions of the design variables and the material properties, it turns out that the intermediate design variables occur due to the differences in the interpretation of the Young's modulus and the Darcy's force. As a penalization factor of the Darcy's force (3 for the SIMP) is higher than the penalization factor of the Young's modulus (5 for the SIMP), the intermediate design variables become effective; in the present example, 8 for the mass penalization is employed to remove the large deformation due to the inertia force. To overcome this, it is possible to have a lower penalization factor for the Darcy's force but it causes another non-convergence.

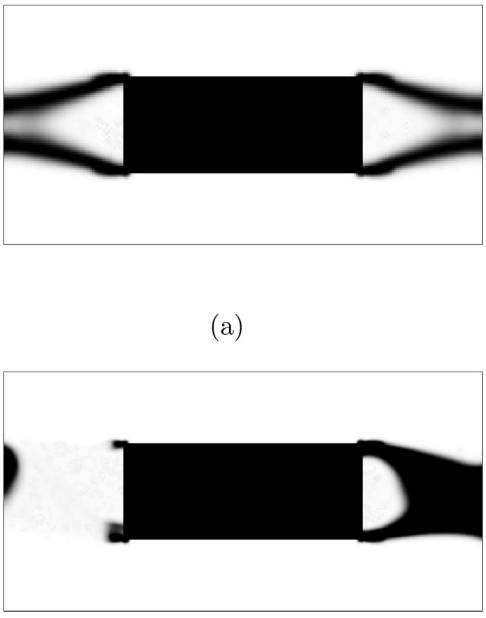

Fig. 13. Optimized layouts with a refined mesh (424 by 210 discretization).

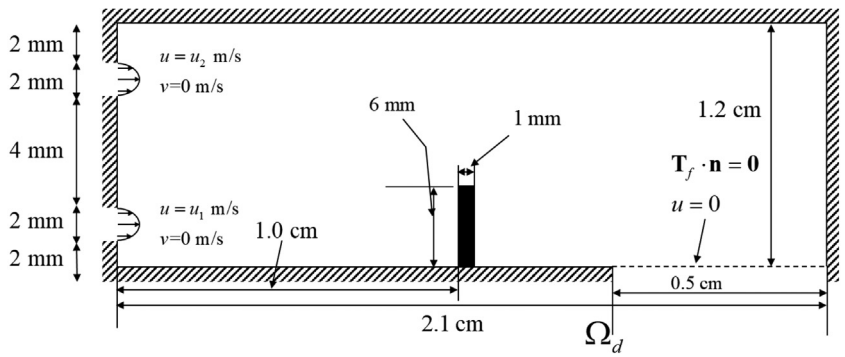

Fig. 14. Example 3: Problem definition (110 by 60 discretization, $\rho_s = 7800$ kg/m^3, Young's modulus: 200×10^9 Pa, $\rho_f = 1000$ kg/m^3, $\mu = 1$ Pa s, $\alpha_{\max} = 10^9$ Pa $\frac{\text{s}}{\text{m}^2}$, mass: 5%, $n = 3$, $n_s = 8$, $n_{filter} = 7$, $n_{per} = 7$, Initial value $= 0.2$, 10% mass constraint).

4. Conclusions

This study focused on the development and exploitation of a topology optimization scheme for a transient FSI system using a monolithic design approach. With conventional analysis procedures for the FSI system, the optimization procedure becomes complex because the governing equations should be interpolated with respect to the design variables. Regarding the importance of optimizing a complex multiphysics system, the monolithic design

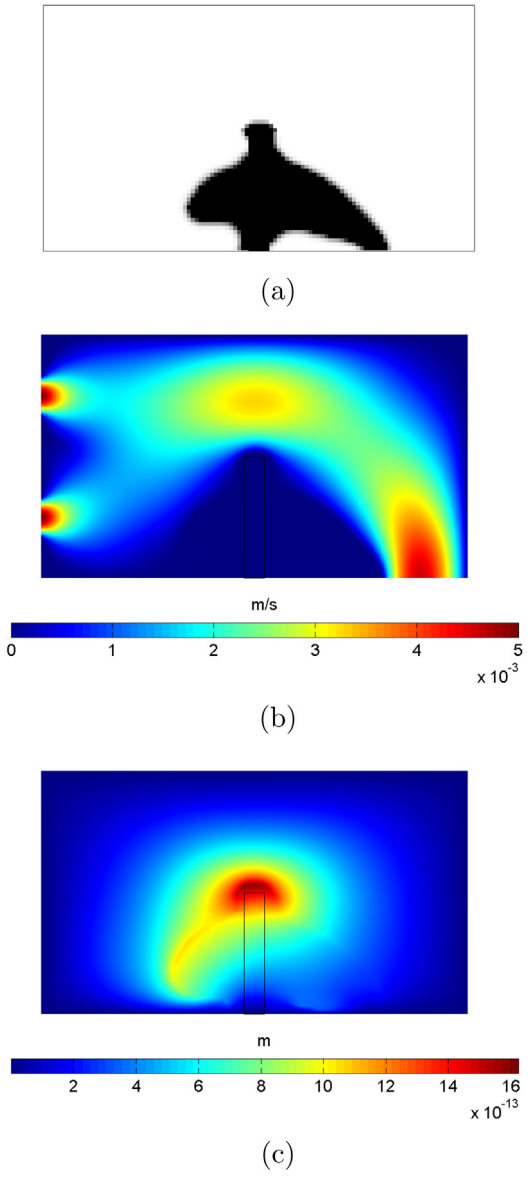

Fig. 15. Optimized layout with the boundary condition. (a) The optimized layout ($u_{in}^1 = t \times s_1$ m/s, $u_{in}^2 = t \times s_2$ m/s, $u_0 = 2\times10^{-3}$ m/s, $s_1 = u_0 \times \frac{\left(3\times10^{-3}-y\right)\left(y-10^{-3}\right)}{\left(2\times10^{-3}\right)^2/4}$, $s_2 = u_0 \times \frac{\left(9\times10^{-3}-y\right)\left(y-7\times10^{-3}\right)}{\left(2\times10^{-3}\right)^2/4}$ m/s), (b) the fluid velocity and (c) the structural displacements. (For interpretation of the references to color in this figure legend, the reader is referred to the web version of this article.)

approach models the pseudo-void structural domain for the fluid domain in the linear elasticity equation and the pseudo-solid minimizing the penetration of fluid for the solid domain in the Navier–Stokes equation. The mutual coupling boundary conditions were transferred and modeled using the divergence theory and deformation tensor in the monolithic design approach with time-varying terms. The variational form was used for the adjoint sensitivity analysis. Several examples were solved to demonstrate the validity of the proposed formation. On logical grounds,

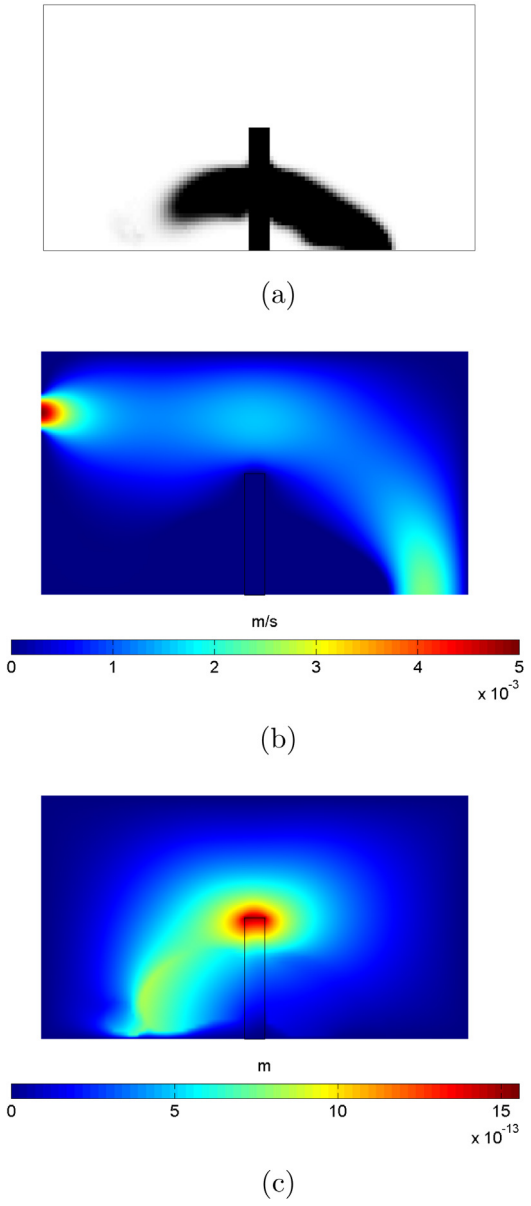

Fig. 16. Optimized layout with the boundary condition. (a) The optimized layout, ($u_{in}^1 = (1-t) \times s_1$ m/s, $u_{in}^2 = t \times s_2$ m/s, $u_0 = 2\times10^{-3}$ m/s, $s_1 = u_0 \times \frac{\left(3\times10^{-3}-y\right)\left(y-10^{-3}\right)}{\left(2\times10^{-3}\right)^2/4}$, $s_2 = u_0 \times \frac{\left(9\times10^{-3}-y\right)\left(y-7\times10^{-3}\right)}{\left(2\times10^{-3}\right)^2/4}$ m/s), (b) the fluid velocity and (c) the structural displacements. (For interpretation of the references to color in this figure legend, the reader is referred to the web version of this article.)

there is no compelling reason to argue that the effects of the time-varying boundary conditions on topologically optimized layouts can be observed. By varying the magnitude and direction of the input fluid velocity, an optimized layout can be obtained, and the integration value of the time-varying compliance can be improved. The findings of relevant studies on transient fluids support this claim. In future research, developments should be made to consider

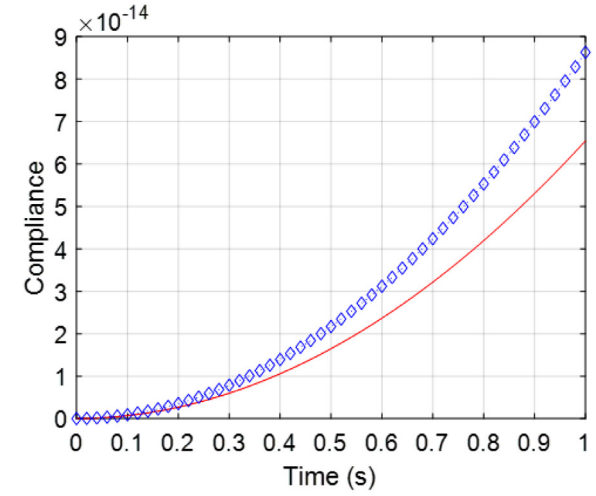

(a)

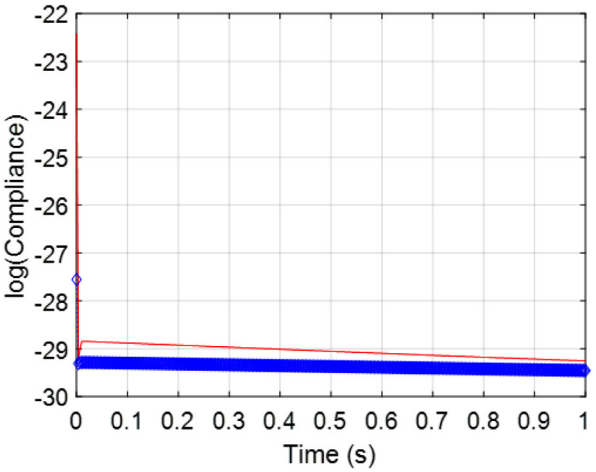

(b)

Fig. 17. Recomputed compliance comparison for each boundary condition. (a) Reanalysis of the optimized layouts with the boundary condition in Fig. 15 (red line: the response in Fig. 15 and 1.0945 $\times 10^{-14}$ J, blue dotted line: the response in Fig. 16 and 1.2206 $\times 10^{-14}$ J), and (b) reanalysis of the optimized layouts with the boundary condition in Fig. 16 (red line: the response in Fig. 16 and 5.4894 $\times 10^{-14}$ J s, blue dotted line: the response in Fig. 15 and 5.4975 $\times 10^{-14}$ J s). (For interpretation of the references to color in this figure legend, the reader is referred to the web version of this article.)

the interaction between the structure and turbulent flow. As the turbulent flow oscillates with respect to time, time-varying fluctuations of the structure must be considered. In short, this study considered a transient FSI system for topology optimization.

Declaration of competing interest

The authors declare that they have no known competing financial interests or personal relationships that could have appeared to influence the work reported in this paper.

Data availability

Data will be made available on request.

Funding information

This work was supported by a National Research Foundation of Korea (NRF) grant funded by the Korean government (MSIT) (NRF-2019R1A2C2084974).

References

[1] M.P. Bendsoe, O. Sigmund, Topology Optimization: Theory, Methods, and Applications, second ed., Springer-Verlag Berlin Heidelberg, 2004.
[2] M.Y. Wang, X. Wang, D. Guo, A level set method for structural topology optimization, Comput. Methods Appl. Mech. Engrg. 192 (1) (2003) 227–246.
[3] W. Zhang, D. Li, J. Zhou, Z. Du, B. Li, X. Guo, A moving morphable void (MMV)-based explicit approach for topology optimization considering stress constraints, Comput. Methods Appl. Mech. Engrg. 334 (2018) 381–413.
[4] H. Zhang, A. Takezawa, X. Ding, S. Xu, H. Li, H. Guo, Topology optimization of degradable composite structures with time-changeable stiffness, Internat. J. Numer. Methods Engrg. 122 (17) (2021) 4751–4773.
[5] X.Y. Chen, Topology optimization of microfluidics - A review, Microchem. J. 127 (2016) 52–61.
[6] A. Ghasemi, A. Elham, Efficient multi-stage aerodynamic topology optimization using an operator-based analytical differentiation, Struct. Multidiscip. Optim. 65 (130) (2022).
[7] R. Picelli, E. Moscatelli, P.V.M. Yamabe, D.H. Alonso, S. Ranjbarzadeh, R. dos Santos Gioria, J.R. Meneghini, E.C.N. Silva, Topology optimization of turbulent fluid flow via the TOBS method and a geometry trimming procedure, Struct. Multidiscip. Optim. 65 (34) (2022).
[8] Y. Deng, Z. Liu, P. Zhang, Y. Liu, Y. Wu, Topology optimization of unsteady incompressible Navier–Stokes flows, J. Comput. Phys. 230 (17) (2011) 6688–6708.
[9] S. Zhou, Q. Li, A variational level set method for the topology optimization of steady-state Navier–Stokes flow, J. Comput. Phys. 227 (24) (2008) 10178–10195.
[10] D. Makhija, G. Pingen, R. Yang, K. Maute, Topology optimization of multi-component flows using a multi-relaxation time lattice Boltzmann method, Comput. & Fluids 67 (2012) 104–114.
[11] P. He, C.A. Mader, J.R. Martins, K.J. Maki, An aerodynamic design optimization framework using a discrete adjoint approach with OpenFOAM, Comput. & Fluids 168 (2018) 285–303.
[12] J. Yan, R. Xiang, D. Kamensky, M.T. Tolley, J.T. Hwang, Topology optimization with automated derivative computation for multidisciplinary design problems, Struct. Multidiscip. Optim. 65 (2022) 114406.
[13] C.M. Okubo, L.F. Sá, C.Y. Kiyono, E.C. Silva, A discrete adjoint approach based on finite differences applied to topology optimization of flow problems, Comput. Methods Appl. Mech. Engrg. 389 (2022) 114406, http://dx.doi.org/10.1016/j.cma.2021.114406.
[14] L.C. Høghøj, D.R. Nørhave, J. Alexandersen, O. Sigmund, C.S. Andreasen, Topology optimization of two fluid heat exchangers, Int. J. Heat Mass Transfer 163 (2020) 120543.
[15] A. Evgrafov, G. Pingen, K. Maute, Topology optimization of fluid domains: Kinetic theory approach, ZAMM - J. Appl. Math. Mech. 88 (2008) 129–141.
[16] E.M. Papoutsis-Kiachagias, K.C. Giannakoglou, Continuous adjoint methods for turbulent flows, applied to shape and topology optimization: Industrial applications, Arch. Comput. Methods Eng. 23 (2) (2016) 255–299.
[17] C.M. Okubo, C.Y. Kiyono, L.F. Sá, E.C. Silva, Topology optimization applied to 3D rotor flow path design based on the continuous adjoint approach, Comput. Math. Appl. 96 (2021) 16–30.
[18] G.H. Yoon, Topology optimization method with finite elements based on the k-ε turbulence model, Comput. Methods Appl. Mech. Engrg. 361 (2020) 112784.
[19] G.H. Yoon, Topology optimization for turbulent flow with Spalart–Allmaras model, Comput. Methods Appl. Mech. Engrg. 303 (2016) 288–311.
[20] X. Qian, E.M. Dede, Topology optimization of a coupled thermal-fluid system under a tangential thermal gradient constraint, Struct. Multidiscip. Optim. 54 (3) (2016) 531–551.
[21] X. Zhao, M. Zhou, Y. Liu, M. Ding, P. Hu, P. Zhu, Topology optimization of channel cooling structures considering thermomechanical behavior, Struct. Multidiscip. Optim. 59 (2) (2019) 613–632.
[22] A.K. Datta, Porous media approaches to studying simultaneous heat and mass transfer in food processes. I: Problem formulations, J. Food Eng. 80 (1) (2007) 80–95.
[23] E.M. Dede, Optimization and design of a multipass branching microchannel heat sink for electronics cooling, J. Electron. Pack. 134 (4) (2012).
[24] E.M. Dede, J. Lee, Y. Liu, B. Robert, S.H. Yonak, Computational methods for the optimisation and design of electromechanical vehicle systems, Int. J. Veh. Des. 58 (2–4) (2012) 159–180.
[25] A.A. Koga, E.C.C. Lopes, H.F.V. Nova, C.R. de Lima, E.C.N. Silva, Development of heat sink device by using topology optimization, Int. J. Heat Mass Transfer 64 (2013) 759–772.

[26] E.A. Kontoleontos, E.M. Papoutsis-Kiachagias, A.S. Zymaris, D.I. Papadimitriou, K.C. Giannakoglou, Adjoint-based constrained topology optimization for viscous flows, including heat transfer, Eng. Optim. 45 (8) (2013) 941–961.
[27] K. Yaji, T. Yamada, M. Yoshino, T. Matsumoto, K. Izui, S. Nishiwaki, Topology optimization in thermal-fluid flow using the lattice Boltzmann method, J. Comput. Phys. 307 (2016) 355–377.
[28] T. Dbouk, A review about the engineering design of optimal heat transfer systems using topology optimization, Appl. Therm. Eng. 112 (2017) 841–854.
[29] M. Pietropaoli, F. Montomoli, M. Gaymann, Three-dimensional fluid topology optimization for heat transfer, 59 (3) (2019) 801–812.
[30] E.M. Dede, J. Lee, T. Nomura, Multiphysics Simulation: Electromechanical System Applications and Optimization, Springer-Verlag London, 2014.
[31] S.-H. Ha, S. Cho, Topological shape optimization of heat conduction problems using level set approach, Numer. Heat Transfer B 48 (1) (2005) 67–88.
[32] J. Alexandersen, N. Aage, C.S. Andreasen, O. Sigmund, Topology optimisation for natural convection problems, Internat. J. Numer. Methods Fluids 76 (10) (2012) 699–721.
[33] S. Das, A. Sutradhar, Multi-physics topology optimization of functionally graded controllable porous structures: Application to heat dissipating problems, Mater. Des. 193 (2020) 108775, http://dx.doi.org/10.1016/j.matdes.2020.108775.
[34] G.H. Yoon, Transient sensitivity analysis and topology optimization for particle motion in steady state laminar fluid, Comput. Methods Appl. Mech. Engrg. 367 (2020) 113096.
[35] C.S. Andreasen, A framework for topology optimization of inertial microfluidic particle manipulators, Struct. Multidiscip. Optim. (2020).
[36] G.H. Yoon, Topology optimization for stationary fluid-structure interaction problems using a new monolithic formulation, Internat. J. Numer. Methods Engrg. 82 (5) (2010) 591–616.
[37] G.H. Yoon, Stress-based topology optimization method for steady-state fluid–structure interaction problems, Comput. Methods Appl. Mech. Engrg. 278 (2014) 499–523.
[38] D.J. Munk, D. Verstraete, G.A. Vio, Effect of fluid-thermal-structural interactions on the topology optimization of a hypersonic transport aircraft wing, J. Fluids Struct. 75 (2017) 45–76.
[39] H. Li, T. Kondoh, P. Jolivet, K. Furuta, T. Yamada, B. Zhu, K. Izui, S. Nishiwaki, Three-dimensional topology optimization of a fluid–structure system using body-fitted mesh adaption based on the level-set method, Appl. Math. Model. 101 (2022) 276–308.
[40] A. Neofytou, F. Yu, L. Zhang, H.A. Kim, Level Set Topology Optimization for Fluid-Structure Interactions. URL https://arc.aiaa.org/doi/abs/10.2514/6.2022-2091.
[41] N. Jenkins, K. Maute, Level set topology optimization of stationary fluid-structure interaction problems, Struct. Multidiscip. Optim. 52 (1) (2015) 179–195.
[42] K. Maute, Topology optimization of coupled multi-physics problems, in: Topology Optimization in Structural and Continuum Mechanics, Springer, 2014, pp. 421–437.
[43] K. Maute, G.W. Reich, Integrated multidisciplinary topology optimization approach to adaptive wing design, J. Aircr. 43 (1) (2006) 253–263.
[44] R. Picelli, S. Ranjbarzadeh, R. Sivapuram, R. Gioria, E. Silva, Topology optimization of binary structures under design-dependent fluid-structure interaction loads, Struct. Multidiscip. Optim. 62 (2020) 2101–2116.
[45] R. Picelli, W. Vicente, R. Pavanello, Evolutionary topology optimization for structural compliance minimization considering design-dependent FSI loads, Finite Elem. Anal. Des. 135 (2017) 44–55.
[46] F. Feppon, G. Allaire, C. Dapogny, P. Jolivet, Topology optimization of thermal fluid-structure systems using body-fitted meshes and parallel computing, J. Comput. Phys. 417 (2020) 109574.
[47] K. Svanberg, The method of moving asymptotes – a new method for structural optimization, Internat. J. Numer. Methods Engrg. 24 (2) (1987) 359–373.